Research Square

Preprints are preliminary reports that have not undergone peer review.
They should not be considered conclusive, used to inform clinical practice,
or referenced by the media as validated information.

Antimicrobial activity and rice germination potency of Cassia sophera (L.) Roxb. Extracts: an in vitro and in silico study

Md. Sanowar Hossan
University of Rajshahi
Konika Akter Eva
University of Rajshahi
Md. Abdul Momin
University of Rajshahi
Md. Mahedi Hasan Sourov
University of Rajshahi
Md. Naymur Rahman
University of Rajshahi
Md. Nahid Hasan Joy
Gopalganj Science and Technology University
Chandan Barai
University of Rajshahi
Most. Suhita Aktar
University of Rajshahi
Ahmed Saif
University of Rajshahi
Nurul Islam
University of Rajshahi
Meherun Nesa
University of Rajshahi
Md. Faruk Hasan
faruk_geb@ru.ac.bd

University of Rajshahi

Article

Keywords: Cassia sophera, Antimicrobial activity, Rice growth, Molecular docking, CTX-M-9 β-lactamase, In vitro and in silico study

Posted Date: November 10th, 2026

DOI: https://doi.org/10.21203/rs.3.rs-11491255/v1

License: This work is licensed under a Creative Commons Attribution 4.0 International License.
Read Full License

Additional Declarations: No competing interests reported.

Antimicrobial activity and rice germination potency of *Cassia sophera* (L.) Roxb. Extracts: an in vitro and in silico study

Md. Sanowar Hossan[1], Konika Akter Eva[1], Md. Abdul Momin[2], Md. Mahedi Hasan Sourov[2], Md. Naymur Rahman[1], Md. Nahid Hasan Joy[3], Chandan Barai[4], Most. Suhita Aktar[5], Ahmed Saif[6], Nurul Islam[1], Meherun Nesa[1*], Md. Faruk Hasan[2*]

[1] Department of Zoology, University of Rajshahi, Rajshahi 6205, Bangladesh

[2] Department of Microbiology, University of Rajshahi, Rajshahi 6205, Bangladesh

[3] Department of Biotechnology and Genetic Engineering, Gopalganj Science and Technology University, Gopalganj 8105, Bangladesh

[4] Department of Biochemistry and Molecular Biology, University of Rajshahi, Rajshahi 6205, Bangladesh

[5] Department of Chemistry, University of Rajshahi, Rajshahi-6205, Bangladesh

[6] Department of Pharmacy, University of Rajshahi, Rajshahi, 6205, Bangladesh

***Corresponding authors**

Email: meherunmerry@ru.ac.bd (MN),

faruk_geb@ru.ac.bd (MFH), ORCiD: https://orcid.org/0000-0003-2746-5994

Abstract

Multidrug-resistant (MDR) pathogens pose a major global threat to public health, creating an urgent demand for natural antimicrobial agents. This study evaluated the bioactive potential of *Cassia sophera* against pathogenic bacteria and fungi and conducted phytotoxicity assays using rice seeds. To identify potential *C. sophera*-derived inhibitors targeting CTX-M-9 β-lactamase, we used computational approaches. *In vitro* antibacterial assays revealed that the methanolic extract exhibited the highest inhibitory activity against *Escherichia coli*, with an inhibition zone of 25.79±0.32 mm. The highest antifungal activity was observed against *Fusarium concentricum* with 41.97–45.38% and *F. fujikuroi* with 40.02–41.99% inhibition. The highest seed germination rate was observed at 95.55% in the methanolic extract of *C. sophera.* Molecular docking (MD) studies demonstrated stronger binding affinities for CID 624791 (-8.0 kcal/mol) and CID 5304778 (-7.2 kcal/mol) with the CTX-M-9 β-lactamase (PDB ID: 1YLY), outperforming the reference Ceftazidime (-7.0 kcal/mol). ADME and toxicity analyses indicated that the leading compounds have favorable pharmacokinetic profiles with low predicted toxicity. During 100 ns MD simulations, both compounds maintained stable conformational behavior. MM-PBSA and DFT analysis revealed CID 624791 as a potential candidate with a binding free energy of −25.56 ± 2.54 kcal/mol. Overall, the integrated experimental and computational findings highlight the antimicrobial potential of *C. sophera* extracts and identify CID 624791 as a promising computational candidate for further experimental validation as a potential CTX-M-9 β-lactamase inhibitor.

Keywords *Cassia sophera,* Antimicrobial activity, Rice growth, Molecular docking, CTX-M-9 β-lactamase, *In vitro* and in silico study

Introduction

The prevalence of multidrug-resistant (MDR) microbes is rising at an alarming rate, accompanied by the emergence of novel strains resistant to nearly all available antibiotics. The World Health Organization (WHO) has recognized antimicrobial resistance (AMR) as one of the ten most critical global public health threats [1]. In 2023, over 1.05 million human deaths were directly attributed to AMR, and it is projected to rise to approximately 10 million annually by 2050 if effective interventions are not implemented [1,2]. The emergence of MDR bacteria diminishes the efficacy of antimicrobial treatments, prolongs illness and hospitalization, and increases mortality. Excessive and inappropriate use of antibiotics in human medicine, veterinary practices, and agriculture has been identified as a major driver of AMR, with global antibiotic consumption increasing by 65% between 2000 and 2015, particularly in low- and middle-income countries [3].

Bacterial pathogens are a significant concern in human health and agriculture, while fungal pathogens play important roles in human health and cause significant losses in postharvest crops. In 2014, the Kenyan Government scrapped around 14,000 tons of maize contaminated with aflatoxins, which can infect and spoil a variety of harvested agricultural products, thereby compounding losses and threatening food security [4]. *Fusarium*-infected diseases remain a significant cause of crop losses worldwide, and some species produce mycotoxins that have carcinogenic and other harmful effects on humans and animals [5,6]. Several studies are underway to develop phyto-pharmaceuticals as substitutes for synthetic drugs, with greater effectiveness against resistant pathogens and a strengthened therapeutic potential of phytotherapy [6,7].

Cassia sophera L. (family Caesalpiniaceae), commonly known as "Kasundi" in Bangladesh, is a tropical plant species found in the Indian subcontinent, including Bangladesh [8]. Different parts of the plant have traditional uses for treating ailments such as pityriasis, psoriasis, asthma, acute bronchitis, cough, diabetes, and convulsions in children [9,10]. The multi-component phytochemicals are appropriate for various ailments and may serve as a powerful source of bioactive chemicals for drug development [11]. The leaves and flower extracts of *C. sophera* have been reported to heal wounds and burns caused by bacterial and fungal infections and to exhibit significant antibacterial activity [12,13]. Moreover, leaves of this plant are rich in phenolic compounds with a strong affinity for various molecular targets, especially proteins and glycoproteins, which are responsible for bacterial and fungal resistance, and significantly counteract them [14].

A significant percentage of pharmaceuticals worldwide are derived from medicinal plants, but very few have been used as antimicrobials or antifungals. Hence, plant derivatives are locally available, have lower production costs, and offer greater environmental and economic sustainability. Medicinal uses of phyto-compounds were supported by the incorporation of traditional knowledge and modern research. The synergistic activity of phytochemicals with microorganisms against antibiotics and antifungals reduces reliance on chemical drugs, reduces microbial resistance, and inhibits drug-inactivating enzymes such as β-lactamases, thereby improving the bioavailability of natural drugs for antimicrobial activity without a negative impact [15,16]. Molecular docking and dynamics simulations can be helpful in the discovery of bioactive compounds through computational advances in biology to predict the binding interactions between phytochemicals and target protein complexes over time [17,18].

Extraintestinal pathogenic *Escherichia coli* (ExPEC) primarily causes infections outside the intestines and is associated with the dissemination of antibiotic resistance due to high genetic plasticity [19]. Selected commensal strains in the presence of antimicrobial agents over the host's lifetime make them useful markers of the host-antimicrobial agent relationship [20]. The CTX-M-9 gene has become the most common extended-spectrum β-lactamase (ESBL) in MDR *E. coli*, conferring resistance to β-lactam antibiotics cefotaxime and ampicillin [21]. These antibiotics are clinically prominent, but few effective inhibitors of CTX-M-9 have been identified, and the mechanisms underlying their activity remain unknown [22]. Targeting CTX-M-9 with plant-derived inhibitors may be a promising strategy for developing novel antimicrobial drugs. Hence, the present study aimed to investigate the antimicrobial and growth-modulating effects of *C. sophera* extracts using experimental and computational approaches.

Materials and methods

Experimental study

Collection, identification, and extraction of plant material

We collected *Cassia sophera* from the Rajshahi University campus, Bangladesh. The plant was grown on the roadside of fallow land. During identification, we verbally obtained permission, identified and authenticated the plant as *Cassia sophera* (L.) Roxb. (Voucher No. 43734) from the dataset of the Bangladesh National Herbarium, Mirpur, Dhaka, Bangladesh. Collected aerial parts of *C. sophera* were thoroughly washed to remove adhering impurities. The material was then cut into small pieces and air-dried at room temperature for one week. The plant material was dried and ground mechanically to get a coarse powder. Petroleum ether, chloroform, and methanol were used sequentially in a 1:3 ratio with a total amount of 50 g of *C. sophera* plant powder. Methanol, chloroform, and petroleum ether were used to provide a polarity gradient, ensuring effective

extraction of the phytochemicals. The extraction process was conducted over 7 days with continuous shaking (12 hours per day). Subsequently, the extracts were filtered through Whatman No. 1 filter paper and allowed to dry completely. The dried extracts were stored at 4 °C until further use.

Bacterial strain collection and antibacterial susceptibility test

The antibacterial activity of *C. sophera* extracts was evaluated against several Gram-positive and Gram-negative bacterial strains, including *Staphylococcus aureus* ATCC25923, *Bacillus subtilis* ATCC6633, *Pseudomonas aeruginosa* ATCC27853, *Escherichia coli* ATCC25922, *Serratia marcescens* MT912927, *Shigella sonnei* clinical isolate, *Shigella flexneri* clinical isolate, and *Staphylococcus gallinarum* MT912994. The bacterial strains were obtained from the Microbiology and Biotechnology Research Lab., Department of Microbiology, University of Rajshahi, Bangladesh. Antibacterial efficacy was determined using the disc diffusion method following a previously described protocol [23]. The crude extracts prepared in petroleum benzene, chloroform, and methanol were tested for their inhibitory activity. Sterile paper discs (6 mm in diameter) were impregnated with 50, 100, and 200 µg/disc of plant extracts. The prepared discs were placed onto Luria–Bertani (LB) agar plates inoculated with freshly cultured bacterial suspensions. Inoculum was prepared by incubating bacterial cultures in LB broth at 37 °C for 24 h. A total of 50 µL of bacterial inoculum (2.5×10^6 CFU/mL) was plated onto 90-mm Petri dishes containing 20 mL of LB agar medium. Ciprofloxacin (5 µg/disc) was used as the positive control, whereas discs treated with the corresponding solvents served as the negative control. The inoculated plates were incubated at 37 °C for 24 h, and the antibacterial activity was determined by measuring the diameter of the inhibition zones (mm) surrounding the discs.

Fungal strain collection and antifungal susceptibility test

The antifungal activity of *C. sophera* extracts was evaluated within two fungal species, including *Fusarium fujikuroi* MT856372 and *Fusarium concentricum* MT856371. Antifungal activity was evaluated by the Kirby-Bauer disc diffusion method [23]. Potato Dextrose agar (PDA) medium was prepared and poured into sterile Petri dishes in a laminar airflow. After solidification of the agar plates, sterile filter paper discs (6 mm diameter) were placed on the agar surface. The discs were moistened with *C. sophera* extracts at concentrations of 50, 100, or 200 µg/disc, prepared in methanol, chloroform, or petroleum benzene at a concentration of 1 µg/µL. Fungal cultures were cut using a sterile cork borer and placed in the center of the agar plate. The fungal plugs were then gently pressed to ensure proper contact, and then the plates were incubated at 27 °C for 120 hours. After the incubation period, the radial growth of the fungal colonies was measured in mm on both control and treated plates. Abbot's formula [27] was used to measure the fungal growth inhibition:

$$\text{Percentage of inhibition} = \frac{\text{Growth in control} - \text{Growth in treatment}}{\text{Growth in control}} \times 100$$

After mycelial growth, fungi were stained with lactophenol cotton blue (LPCB) and observed under a light microscope (40×) to assess whether any morphological changes occurred within the treated plate.

Seed germination and seedling growth assessment

To assay seed germination, 30 BRRI Dhan-28 seeds were washed thoroughly with distilled water, then immersed in 70% ethanol for 2 minutes, followed by treatment with a 1.5% sodium hypochlorite solution for 5 minutes. The seeds were then rinsed four times with distilled water to remove residual chemicals. A single layer of sterile tissue paper immersed in 20 mL of distilled

water and seeds was placed in each Petri dish. Liquid solutions of the *C. sophera* extracts at a concentration of 1 µg/µL were applied to the dishes in volumes of 750 µL and 1000 µL. Petri dishes treated with distilled water alone served as the control. Seeds were allowed to germinate in vitro under dark conditions at 25 °C. Seed germination was monitored daily according to the Association of Official Seed Analysts (AOSA) method [24], and seeds were considered germinated when the radicle reached 2 mm in length. After the sixth day of sowing, the germination percentage for each treatment was calculated using the following formula:

$$\text{Germination percentage} = \frac{\text{Number of germinated seeds}}{\text{Total number of seeds}} \times 100$$

After 15 days, seedlings were sampled to record germination percentage, seedling length, and other growth parameters.

In silico study

Protein structure retrieval and preparation

CTX-M-9 β-lactamase protein (PDB ID: 1YLY) was selected as the molecular docking target due to its well-established role in mediating antibiotic resistance in *Escherichia coli*. Its three-dimensional structure, determined by X-ray crystallography at a resolution of 1.25 Å and co-crystallised with a ceftazidime-like boronic acid inhibitor, was obtained from the RCSB Protein Data Bank. Prior to docking analysis, the protein structure was preprocessed by removing crystallographic water molecules and other heteroatoms using Discovery Studio (version 21.1.0). Structural refinement was subsequently performed by adding missing hydrogen atoms, correcting bond orders, and optimizing side-chain conformations. Minimization of energy was then performed using the GROMOS 43B1 force field implemented in Swiss-PDB Viewer. Finally, the optimized protein structure was converted to PDBQT format to facilitate molecular docking using PyRx, which integrates AutoDock Vina.

Ligand preparation

Phytochemicals from *Cassia sophera*, along with ceftazidime as a positive control, were identified through an extensive literature review and database analysis. A total of 51 phytochemicals were selected based on their reported biological activities. Among them, leading compounds were recovered from the PubChem database in three-dimensional SDF (3D-SDF) format. AutoDock Vina software was used to minimize ligand energy using the MMFF94 force field and the steepest-descent algorithm for 2000 steps.

Prediction of the active site

The active site of the amino acid residues of 1YLY was identified using the CASTp server [25]. CASTp provides in-depth quantitative analysis of protein surface features and enables accurate mapping and measurement of three-dimensional structural characteristics (**Fig. 1**).

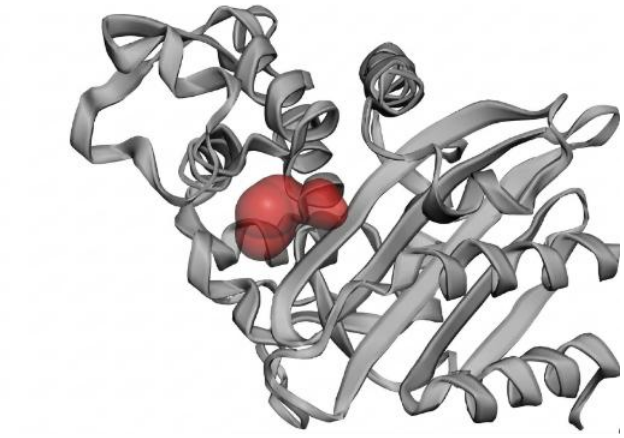


Fig. 1. The active site of the target protein (PDB ID: 1YLY), highlighted in red.

Molecular docking analysis

Molecular docking was used to estimate the binding energy between small molecules and target proteins [26]. The selected phytochemicals of *C. sophera* were docked against the target protein 1YLY using PyRx (AutoDock Vina). The binding sites predicted through CASTp analysis were used to define the docking grid. The axis of the grid box was X = -13.831864, Y = 91.121182, and Z = 53.822909, and the box dimensions were 8.2540 Å, 9.1114 Å, and 8.7206 Å along the X, Y, and Z axes, respectively. This configuration enabled the ligand to explore and actively bind within the target receptors. The negative binding affinities reflected strong protein-ligand interactions and were reported in kcal/mol, and the docking score was ranked by binding score. Finally, two compounds with the highest binding affinities were selected for further analysis. To validate the protocol, the co-crystallised ligand (CB4) was docked into the target protein using the same grid box coordinates. Discovery Studio software was also used to visualize the protein-ligand complexes.

Pharmacokinetics and toxicity assessment

As pharmacokinetics and toxicity are two important parameters for drug safety, therapeutic effectiveness, appropriate dosing strategies, and regulatory acceptability of new drugs [27]. Pre-assessment of compound structural stability and efficacy through pharmacokinetic and toxicity profiling is crucial to the in silico drug discovery process. To examine the pharmacokinetic characteristics of the selected phytochemicals at a preliminary stage, the SwissADME server was employed (https://www.swissadme.ch/) [28]. It offers a comprehensive evaluation of the pharmacokinetic properties and key characteristics of small molecules. Moreover, toxicity assessment is a critical requirement in drug development and design. Accordingly, the toxicity profiles of the selected compounds were evaluated using the ProTox-III server (https:// tox.charite.de/protox_III) [29].

Molecular Mechanics Poisson-Boltzmann Surface Area (MM-PBSA) analysis

The MM-PBSA analysis was performed to estimate the binding free energy of interaction between the selected compounds and the target protein (PDB ID: 1YLY). The binding free energy (ΔG) was calculated using Equation (1) with the MMPBSA.py module of the AMBER molecular dynamics package [30]. This method considers several energy components that contribute to

molecular binding, including both bonded and non-bonded interactions, such as electrostatic interactions, dihedral energy, and van der Waals forces.

$\Delta G = G_{complex} - G_{receptor} - G_{ligand}$

The free energies of the complex, receptor, and ligand are represented by the terms G-complex, G-receptor, and G-ligand, respectively [31].

Density functional theory (DFT) analysis

DFT is widely recognized as a reliable method to study electronic structure and electron distribution within molecular systems [32]. It provides a molecular description and prediction of physical and chemical properties that are important for understanding the interaction mechanism of small molecules with biological receptors in drug discovery [33]. Both CID 5304778 and CID 624791, along with ceftazidime, were optimized using the Gaussian 09W software package [34]. The electronic properties of the selected compounds were computed in their singlet ground state, without considering solvent or charge effects, using the B3LYP functional within the DFT framework and the 6-311++G(d,p) basis set. The combination of functional and basis set is known for its high reliability in optimizing organic molecules with low computational cost [35.] Various global reactivity descriptors, including ionization potential (IP), electron affinity (EA), chemical potential (μ), electronegativity (χ), electrophilicity index (ω), chemical hardness (η), and softness (S), were subsequently derived to assess the reactivity and stability of the studied molecules. All these parameters are derived using the following equations (1-6) [36].

$$\Delta E = \varepsilon_{LUMO} - \varepsilon_{HOMO} \quad (1)$$

$$\chi = -\frac{1}{2}(\varepsilon_{LUMO} + \varepsilon_{HOMO}) \quad (2)$$

$$\mu = \frac{1}{2}(\varepsilon_{LUMO} + \varepsilon_{HOMO}) \quad (3)$$

$$\eta = \frac{1}{2}(\varepsilon_{LUMO} - \varepsilon_{HOMO}) \quad (4)$$

$$S = \frac{1}{2\eta} \quad (5)$$

$$\boldsymbol{\omega} = \frac{\mu^2}{2\eta} \quad (6)$$

Molecular dynamics simulation analysis

Molecular dynamics (MD) simulations provide detailed atomistic insights into the dynamic behavior of molecules and atoms within a simulated system. This computational approach also enables the evaluation of the structural stability of protein–ligand complexes over time [37]. MD simulations were performed to assess the stability of the protein–ligand complexes using the GROMACS 2025.2 software package [38,39]. Protein topologies were generated using the CHARMM36 force field [40], while ligand parameters were derived from the CHARMM General Force Field (CGenFF) [41]. The protein was placed in a rhombic dodecahedral simulation box with dimensions of 8.09 × 8.09 × 5.72 nm and a minimum solute box edge distance of 10 Å. Na^+ and Cl^- ions were added to neutralize the system, and the physiological salt concentration (0.15 M)

was maintained. Energy was minimized under NPT conditions at 300 K and 1 bar pressure utilizing the steepest descent algorithm for up to 50,000 steps until reaching force convergence, which was followed by a two-step equilibration protocol spanning 100 ps across NVT and NPT ensembles with heavy-atom position restraints maintained through the velocity-rescaling (V-rescale) [42] thermostat and the Berendsen barostat with isotropic cell scaling [43]. Long-range electrostatic and short-range interactions were handled via the Particle Mesh Ewald (PME) method with precise Fourier grid spacing and real-space cutoffs, smoothly switched van der Waals interaction ranges, and the LINCS algorithm applied to constrain all bonds involving hydrogen atoms [44]. The MD simulation was carried out within a 100 ns timeframe, and trajectory data were recorded at 10 ps intervals, generating a total of 1000 frames. The stability and flexibility of the complex were assessed using several structural parameters, such as root mean square deviation (RMSD), root mean square fluctuation (RMSF), radius of gyration (Rg), solvent-accessible surface area (SASA), DCCM, FEL, and PCA. The Matplotlib library in Python was used to visualize the MD simulation trajectories.

Statistical analysis

All experiments were replicated three times, and data were analyzed using SPSS v20.0. Mean and standard errors (M ± SE) were calculated using Duncan's multiple range test (DMRT) at $P \leq 0.05$.

Results

Experimental study

Antibacterial susceptibility screening

Among the plant extracts, the methanolic extract showed the largest zone of inhibition with 25.79±0.32 mm against *Escherichia coli* at 200 µg/disc, followed by 24.98±0.59 mm against *Pseudomonas aeruginosa* at the same concentration. In contrast, all tested bacterial strains were resistant to the petroleum benzene extract of *C. sophera*. Overall, the antibacterial effectiveness of the extracts followed the order: methanolic extract > chloroform extract > petroleum benzene extract. Details are provided in **Figs. 2, 3, and S1**.

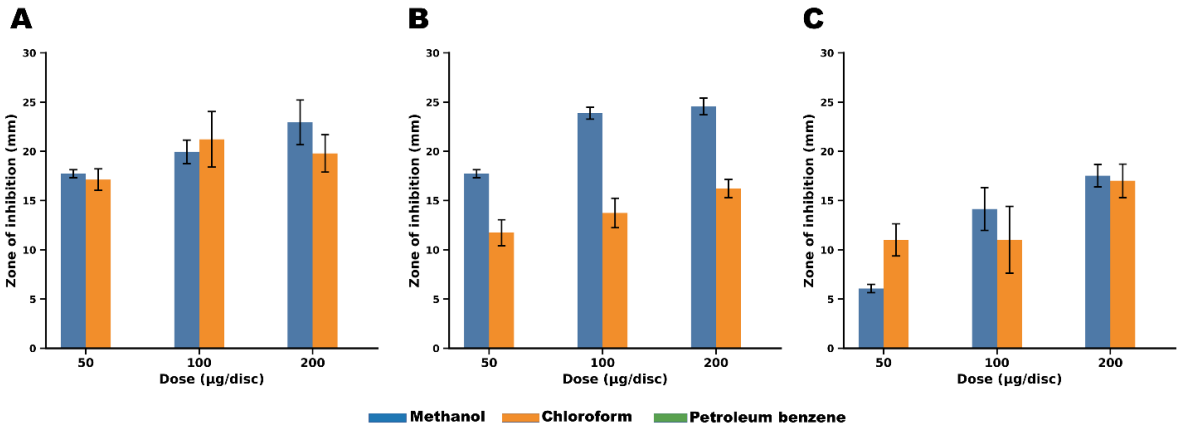


Fig. 2. Zone of inhibition against Gram-positive bacteria. (A) *S. aureus*, (B) *S. gallinarum*, (C) *B. subtilis*, with different solvents and different doses.

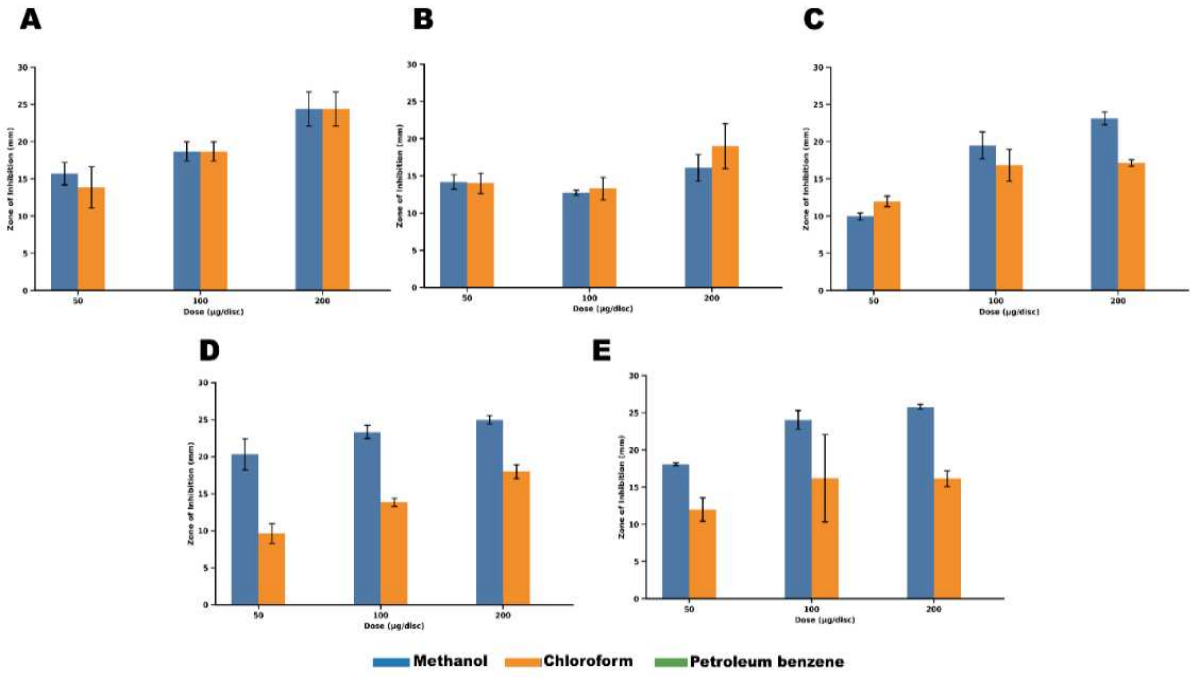


Fig. 3. Zone of inhibition against Gram-negative bacteria. (A) *S. marcescens*, (B) *S. sonnei*, (C) *S. flexneri*, (D) *P. aeruginosa*, and (E) *E. coli* with different solvents and different doses.

Antifungal susceptibility screening

The antifungal activity of *C. sophera* extracts varied significantly with solvent, concentration, and fungal species (**Supplementary Tables S1-S2 and 2; Fig. 4**). Against *F. concentricum*, the methanolic extract showed the highest inhibition (41.97 ± 6.28–45.38 ± 5.05%), with maximum activity at 200 µg/disc (45.38 ± 5.05%). The chloroform extract showed moderate inhibition (34.90–39.16%), whereas petroleum benzene showed lower activity (15.38–22.65%). In contrast, *F. fujikuroi* was most susceptible to the petroleum benzene extract, with inhibition ranging from 40.02 ± 2.78% to 41.99 ± 6.29%, followed by the chloroform extract (34.40–38.41%) and methanolic extract (29.67–33.26%). Under the microscope, the hyphae of the untreated control remained intact and dense and filled with cellular contents for *F. concentricum* and *F. fujikuroi* fungi (**Fig. 5F- H**). However, the treated samples exhibited evident structural damage, including vacuole formation, hyphal rupture, and split, hair-like fragmentation, indicating a considerable cellular disturbance (**Fig. 5 M-P**).

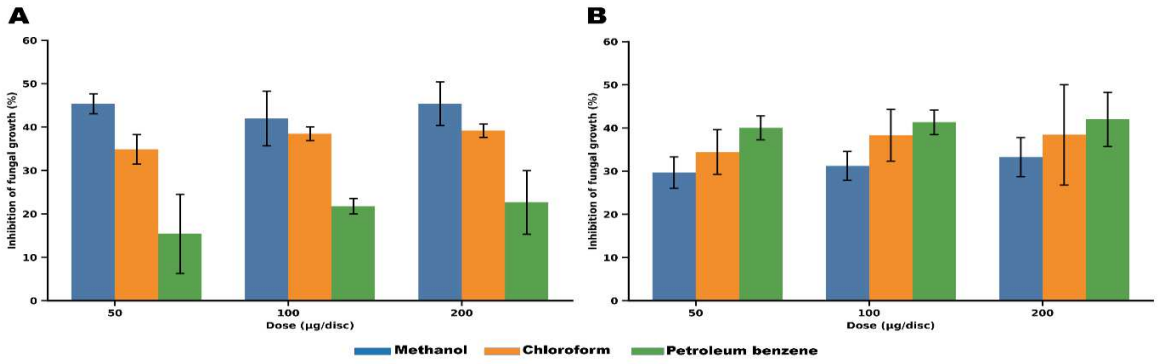


Fig. 4. Mycelium growth inhibition percentage by plant extracts. (A) *Fusarium concentricum*, (B) *F. fujikuroi* growth with different solvents and different doses.

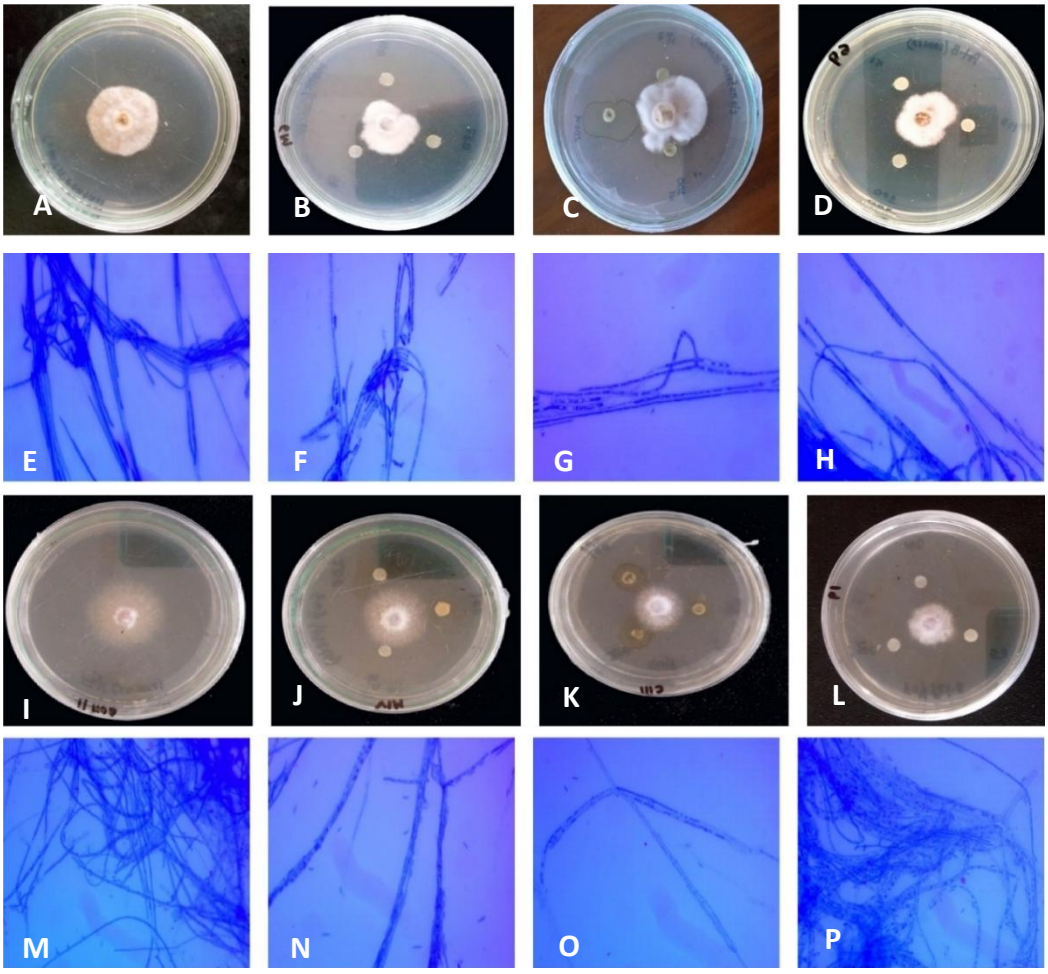


Fig. 5. Antifungal activity of plant extracts against *Fusarium concentricum* and *Fusarium fujikuroi*. **(**A-D) *F. concentricum* culture under control, methanol, chloroform, and petroleum benzene extracts; (F-H) *F. concentricum* staining grown under control, methanol, chloroform, and petroleum benzene extracts; (I-L) *F. fujikuroi* culture under control, methanol, chloroform, and petroleum benzene extracts, and (M-P) *F. concentricum* staining grown under control, methanol, chloroform, and petroleum benzene extracts.

Seed germination and seedling growth

The efficacy of *Cassia sophera* extracts synthesized using different solvents on the germination percentage of 30 BRRI Dhan-28 seedlings is presented in **Fig. 6A**. The germination rate for the methanolic extract treatment was 95.55%, slightly higher than the control (91.11%). However, the germination percentages of seeds treated with chloroform and petroleum benzene extracts were quite low, ranging from 83.33% to 85.55%. The average root lengths of seedlings after different solvent treatments are presented in **Fig. 6B and Table S3**. Root length of seedlings treated with methanol and chloroform extracts was almost similar to the control with 4.91±1.34 cm, showing a minimum effect on root growth. Conversely, the petroleum benzene extracts reduced root length, with the lowest mean root length of 3.28 ± 0.97 cm observed at the highest concentration of 1000 µg/mL. Shoot length measurements are presented in **Fig. 6C and Table S4**. Seedlings treated with methanol and chloroform extracts exhibited shoot lengths similar to those of the control, with a length of 7.37 ± 0.89 cm. However, petroleum benzene extract showed reduced shoot growth at higher concentrations, with the lowest shoot length recorded as 6.53 ± 0.18 cm at the concentration of 1000 µg/mL (**Table S5 and Fig. S3**).

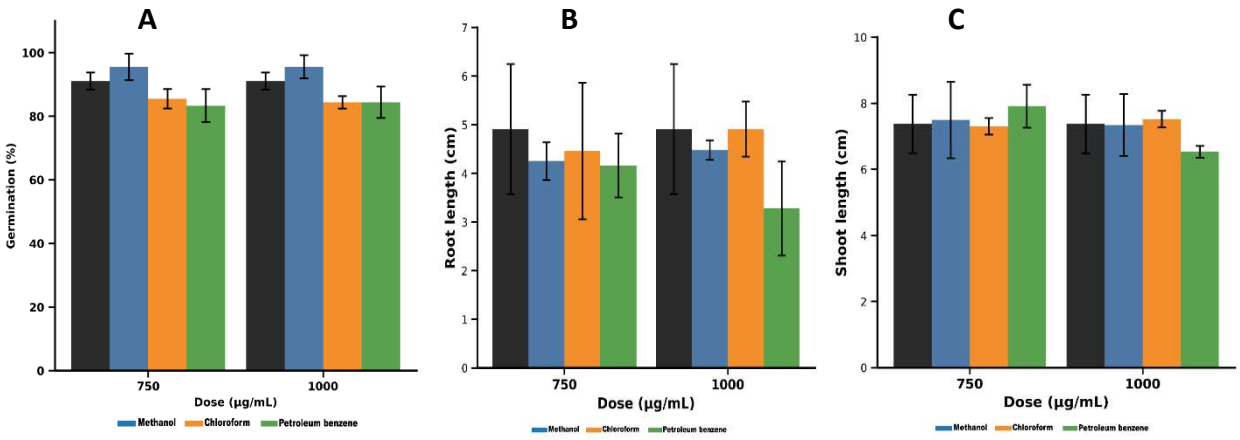


Fig. 6. Effects of plant extracts on rice growth. (A) Percentage of seed germination, (B) Root length of seedlings, and (C) Shoot length of the seedlings with different solvents at different doses.

In silico study

Active site identification

The active binding pocket of the target protein was characterized using the CASTp server, which enabled the identification of key residues within the predicted cavity. The analysis revealed that the most prominent pocket, with a calculated surface area of 53.452, contains several critical amino acid residues, including SER70, LYS73, ASN104, TYR105, SER130, ASN132, LYS234, THR235, GLY236, and SER237 (**Fig. 7**).

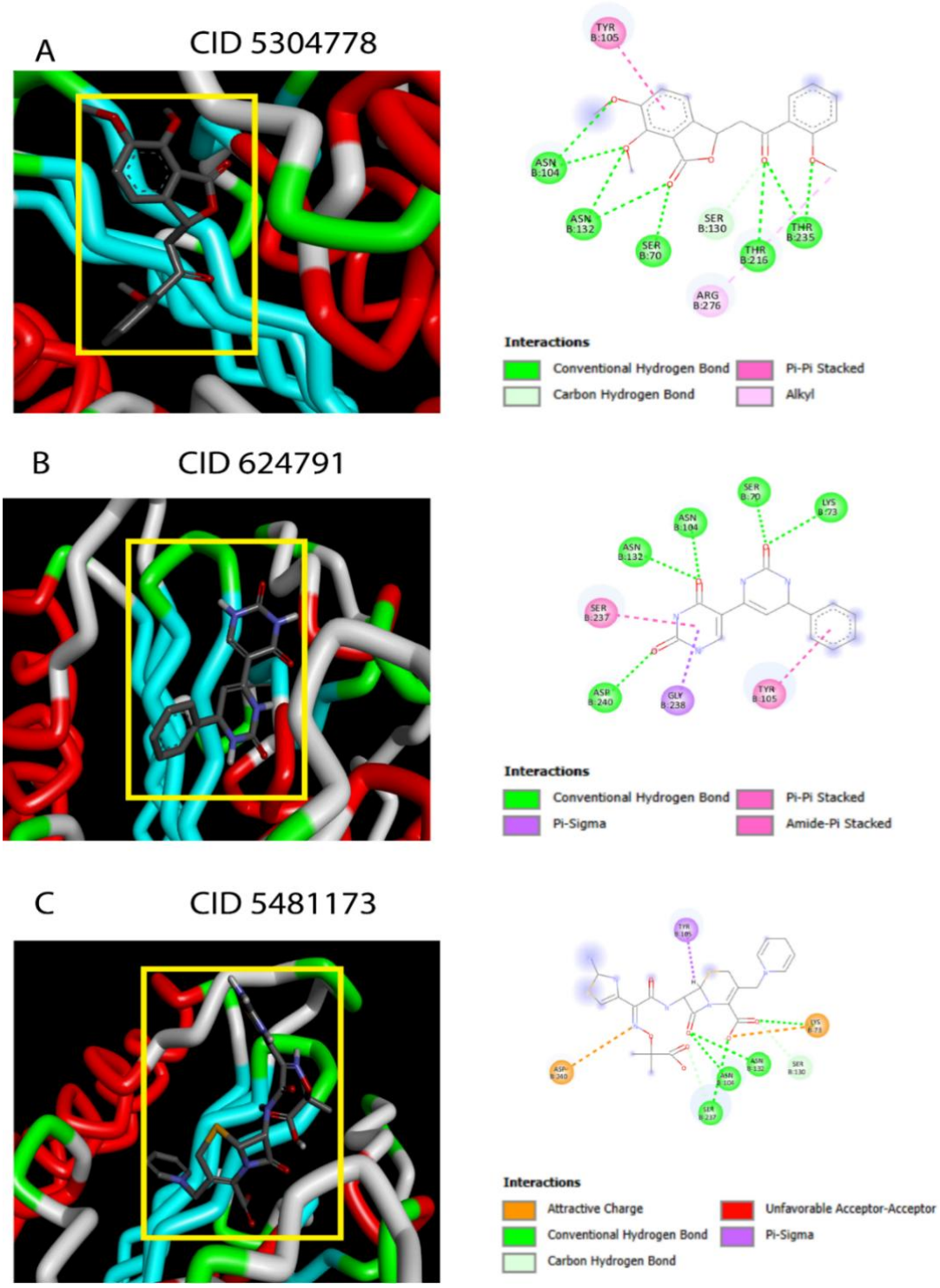


Fig. 7. The protein-ligand interaction, where the 3D interaction is presented on the left and the 2D interaction complex is on the right. Representing the ligands (A) CID 5304778; (B) CID 624791; (C) CID 5481173; with the protein 1YLY.

Molecular docking study

We conducted molecular docking analysis on 51 phytochemicals (**Table S6**) derived from the aerial parts of *C. sophera.* Based on binding affinity values, CID 5304778 and CID 624791 were selected for further analysis compared with the control, CID 5481173 (Ceftazidime). CID 624791 showed the highest binding affinity, with a binding energy of -8.00 kcal/mol, forming five hydrogen bonds with SER70, LYS73, ASN104, ASN132, and ASP240. Similarly, CID 5304778 exhibited a binding energy of -7.2 kcal/mol and formed five hydrogen bonds with the amino acid residues SER70, ASN104, ASN132, THR216, and THR235. Further interactions were detected with various amino acid residues, such as hydrogen, hydrophobic, polar, and π–π stacking interactions (Table 1). On the other hand, ceftazidime showed a binding energy of -7.0 kcal/mol and formed three hydrogen bonds with the amino acid residues ASN104, ASN132, and SER237. The interaction of selected phytocompounds with the target protein revealed that both CID 624791 and CID 5304778 have strong binding affinities, with the highest for CID 624791. Both compounds performed better than the control, Ceftazidime. The range of interactions identified, such as hydrogen and hydrophilic bonds, suggests that these chemicals can efficiently bind to the target protein. Both lead compounds consistently occupied the same binding site as the native co-crystallised ligand, as shown in **Fig. S4**.

Table 1. The docking scores, along with the interacting residues and their corresponding bond types. Additional interaction categories include hydrophobic, van der Waals, π–π stacking, π–sigma, alkyl, and positively and negatively charged interactions.

Compound	Binding affinity (kcal/mol)	Hydrogen bonds	Other interacting bonds
CID 624791	-8.00	SER70, LYS73, ASN104, ASN132, ASP240	TYR105, SER237, GLY238
CID 5304778	-7.2	SER70, ASN104, ASN132, THR216, THR235	TYR105, ARG276, ASN170, LYS73, LYS234, SER237
CID 5481173 (Control)	-7.0	ASN104, ASN132, SER237	TYR105, SER70, GLY236, THR216, THR235, ARG276, ASN170, GLY238

Pharmacokinetic profiling and toxicity assessment

Pharmacokinetics describes the kinetic mechanisms of absorption, distribution, metabolism, and excretion (ADME) [45]. The selected phytocompounds showed good ADME properties (**Table 2**). Moreover, both compounds exhibited minimal toxicity, indicating their potential applicability for safe delivery (**Table 3**).

Table 2. ADME and physicochemical properties of selected lead compounds, including molecular weight, TPSA, LogP, solubility, GI absorption, and BBB permeability.

Parameters	Properties	CID 624791	CID 5304778	CID 5481173
Physiochemical properties	MW (g/mol)	282.25	342.34	546.58
	Heavy atoms	21	25	37
	Aromatic Atoms	18	12	11
	Rotatable bond	2	6	10
	H-bond Acceptors	4	6	9
	H-bond donors	3	0	3
	TPSA (Å2)	111.47	71.06	244.76
Lipophilicity	Log Po/w(Cons)	1.07	2.72	-1.39
Water solubility	Log S (ESOL)	-2.10	-3.57	-1.37
Pharmacokinetics	GI absorption	High	High	Low
	BBB permeant	No	Yes	No
	P-GP substrate	No	No	No
Drug likeness	Lipinski	Yes	Yes	No
Medi. chemistry	Synth. accessibility	2.73	3.44	5.25

Legends: TPSA; topological polar surface area, which predicts drug transport properties; GI absorption; which predicts gastrointestinal absorption (High/Low); BBB permeability; ability to cross the blood–brain barrier; Log P_o/w (Cons); lipophilicity (octanol/water partition coefficient), Log S (ESOL); predicted aqueous solubility; P-gp substrate; indicates if compound is a P-glycoprotein substrate

Table 3. Predicted toxicity profiles of selected compounds, including hepatotoxicity, carcinogenicity, mutagenicity, immunotoxicity, LD_{50} values, and overall toxicity class

Target	CID 624791	CID 5304778	CID 5481173
Hepatotoxicity	Inactive	Inactive	Inactive
Carcinogenicity	Active	Inactive	Inactive
Mutagenicity	Inactive	Inactive	Inactive
Cytotoxicity	Inactive	Inactive	Inactive
LD_{50} (mg/kg)	1000	1500	10000
Immunotoxicity	Inactive	Inactive	Inactive
Toxicity Class	4	4	6

LD_{50}: Median lethal dose (mg/kg), predicts acute toxicity

Density functional theory calculation

Density Functional Theory (DFT) is a reliable quantum-chemical framework for analysing the electronic structure and reactivity of molecules [46]. Frontier Molecular Orbital (FMO) theory, as an integral part of this framework, focuses on the highest occupied molecular orbital (HOMO) and the lowest unoccupied molecular orbital (LUMO), which govern chemical reactivity, charge transfer, and interactions with biological targets [47]. DFT was employed to evaluate key electronic

descriptors, including the energy of HOMO and LUMO, energy gap, ionization potential, electron affinity, chemical potential, electronegativity, hardness, softness, and electrophilicity for CID 5304778, CID 624791, and ceftazidime compounds (**Table 4**). The variation in total energy reflects differences in thermodynamic stability, with lower values indicating greater stability. The ceftazidime compound exhibited the lowest energy with -2503.472 au, compared to the leading compounds CID 624791 and CID 5304778 with -1128.740 au and -984.521 au, respectively. The dipole moment analysis revealed that the ceftazidime compound possessed the highest polarity, followed by CID 624791, while CID 5304778 showed comparatively lower polarity (**Table 1**). Ceftazidime had the highest HOMO value (-5.164 eV), whereas CID 624791 had the lowest (-6.588 eV) (**Fig. S4**). In contrast, the LUMO values suggest that the ceftazidime compound (-3.799 eV) possessed the strongest electron-accepting ability, followed by CID 624791 (-2.884 eV) and CID 5304778 (-1.652 eV). The HOMO–LUMO energy gap varied significantly, with ceftazidime exhibiting the smallest gap (1.365 eV), which ultimately indicates its high reactivity. However, CID 5304778 showed the largest gap of 4.361 eV, and CID 624791 exhibited intermediate behavior with a gap of 3.695 eV. Moreover, the chemical potential and electronegativity values indicate that CID 624791 had a relatively stable electronic environment and a strong electron-attracting ability. As observed earlier, CID 5304778 displayed the lowest electron-attracting ability with an electronegativity of 3.833 eV. The electrophilicity index was highest for the Ceftazidime compound (14.713 eV), confirming its strong electrophilic nature, whereas CID 5304778 exhibited the lowest value (3.369 eV). Ceftazidime compound showed the lowest hardness (0.683 eV) and highest softness (0.732 eV), indicating high reactivity and polarizability, while CID 5304778 was the hardest and least reactive. CID 624791, with moderate hardness (1.848 eV) and softness (0.271), demonstrated a balanced reactivity profile.

Table 4. Calculated global reactivity parameters for the CID 5304778, CID 624791, and Ceftazidime.

Parameters	Compounds		
	CID 5304778	**CID 624791**	**Ceftazidime**
Energy (au)	-1128.740	-984.521	-2503.472
Dipole Moment (D)	5.189	8.928	22.270
HOMO (eV)	-6.014	-6.588	-5.164
LUMO (eV)	-1.652	-2.884	-3.799
Energy Gap (eV)	4.361	3.695	1.365
Ionization Potential (eV)	6.014	6.579	5.164
Electron Affinity (eV)	1.652	2.884	3.799
Chemical Potential (eV)	-3.833	-4.731	-4.482
Electrophilicity (eV)	3.369	6.0582	14.713
Electronegativity (eV)	3.833	4.731	4.482
Hardness (eV)	2.181	1.848	0.683
Softness (eV^{-1})	0.229	0.271	0.732

Molecular dynamics simulations

Molecular dynamics (MD) simulations monitor molecular motions over several time scales and give thermally averaged molecular characteristics that closely match experimental ensemble observations for understanding mechanisms such as molecular binding interactions [48-50]. Various characteristics such as root-mean-square deviation (RMSD), root-mean-square fluctuation

(RMSF), radius of gyration (Rg), solvent-accessible surface area (SASA), dynamic cross-correlation matrix (DCCM), free-energy landscape, and PCA were studied. Both the unbound 1YLY structure and its most favorable compound-bound complex were analyzed.

RMSD analysis of protein–ligand complexes

The RMSD values of protein-ligand complexes are often in the range of 1-3 Å, while greater deviations indicate major conformational rearrangements in the protein structure [51]. Fig. 8A shows the interactions of the target protein (PDB ID: 1YLY) with the studied drugs (CID 624791 and CID 5304778) and the control ceftazidime. The apo protein had an average RMSD of 0.129 nm and a range of 0.0005 to 0.201 nm. The average RMSD of the protein complexed with CID 624791 was 0.151 nm, with a low of 0.0005 nm and a maximum of 0.212 nm. Similarly, the CID 5304778 combination exhibited an average RMSD of 0.158 nm, with values ranging from 0.0005 to 0.297 nm. The regular RMSD of ceftazidime was 0.193 nm, with RMSD values ranging from 0.0005 to 0.307 nm (**Fig. 8A**).

RMSF of protein–ligand complexes

Root mean square fluctuation (RMSF) analysis was performed for each residue in the 1YLY structure across a 100 ns simulation, which identified areas with increased conformational flexibility in the ligand-bound complexes. Significant changes were observed in several residues, including ASP53, LYS88, ASN104, GLY146, THR159, PRO174, GLY217, THR227, GLY255, and ASN271. PRO174 showed the greatest flexibility, with an RMSF of 0.4131 nm. The apo system exhibited highly stable backbone dynamics, with a mean RMSF of 0.0776 nm in the absence of ligand interaction. The average RMSF values were marginally higher for the complexes of CID 624791 and CID 530478 with 0.082893 nm and 0.085667 nm, respectively. On the other hand, the ceftazidime (control) complex exhibited the highest average RMSF of 0.099977 nm. The control has higher RMSF values than the investigated compounds (**Fig. 8B**).

Radius of gyration of protein–ligand complexes

The radius of gyration (Rg) profiles of the complex of ceftazidime (control) with the protein 1YLY, and CID 624791 and CID 530478. The average Rg values of the complexes CID 624791 and CID 530478 were 1.807739 nm and 1.812082 nm, respectively (**Fig. 8C**). The average Rg value for the ceftazidime (control) combination was 1.82791 nm. The lower average Rg values for the investigated compounds compared to the control indicate the creation of more compact protein conformations, whereas the control remained in a stable but relatively less compact structural state throughout the simulation.

SASA analysis of protein–ligand complexes

The solvent-accessible surface area (SASA) analysis of the 1YLY protein during a 100 ns molecular dynamics simulation indicated compound-dependent changes in solvent exposure. The average SASA values of CID 530478, CID 624791, and 1YLY were 115.924 nm^2 and 117.1827 nm^2, respectively. The ceftazidime (control) complex had a slightly higher average SASA value of 118.3647 nm^2 (**Fig. 8D**). The SASA values of both tested drugs were lower than those of the control, indicating relatively better surface accessibility. Collectively, these data suggest that CID 530478 and CID 624791 yield more stable, compact protein structures than ceftazidime in the simulation.

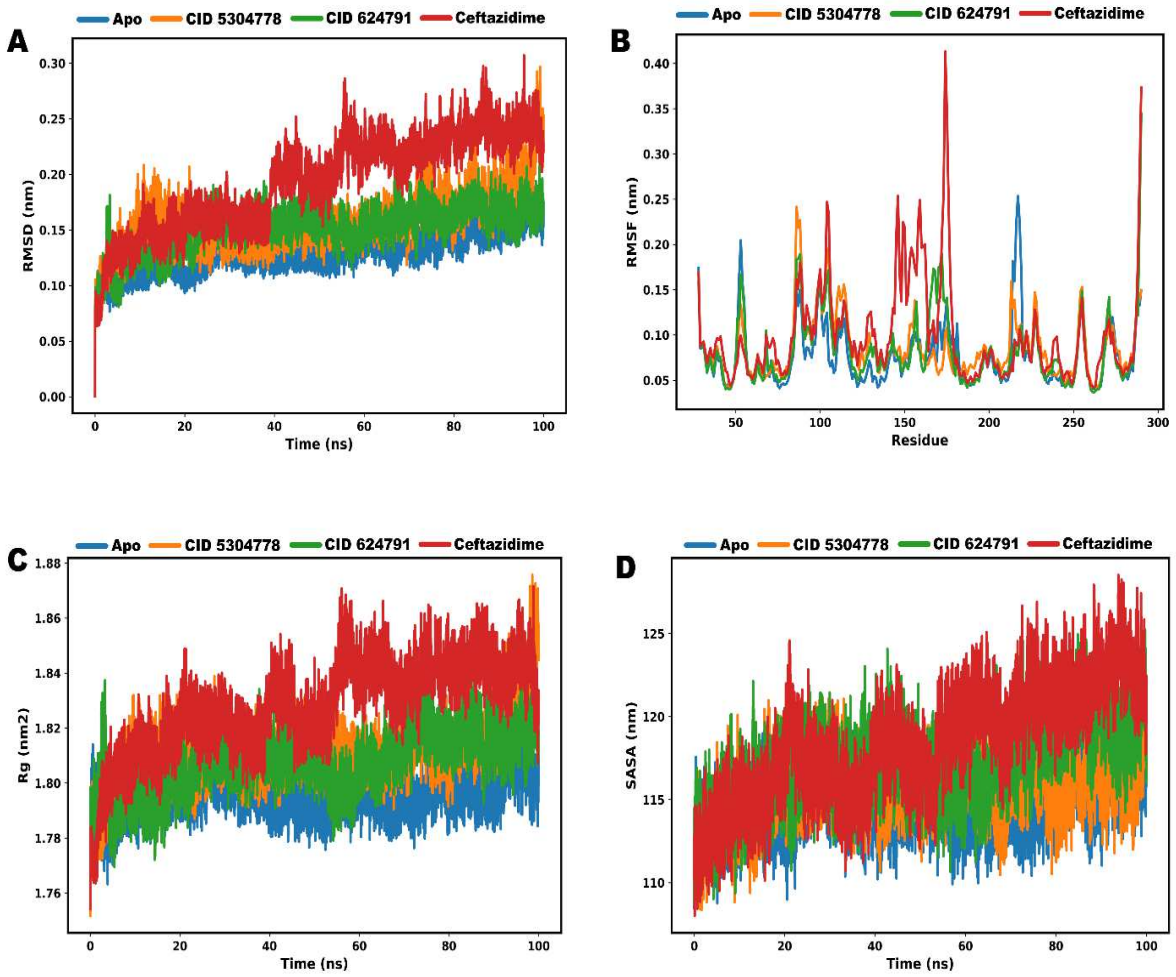


Fig. 8. RMSD analysis of protein–ligand complexes. (A) Cα RMSD, (B) RMSF, (C) Rg, and (D) SASA of 1YLY over 100 ns. Apo is shown in blue; complexes with CID 5304778, CID 624791, and Ceftazidime are shown in orange, green, and red, respectively.

MM-PBSA binding free energy calculation

The MM-PBSA calculation yielded lower binding free energy (DG) values, indicating higher protein-ligand binding affinities. MM-PBSA illustrates the relationship between the standard and the predicted free binding energies for ligands Ceftazidime, CID 624791, and CID 5304778. The average ΔG values for Ceftazidime, CID 624791, and CID 5304778 were -18.37 ± 3.46, -25.56 ± 2.54, and -16.08 ± 4.23 kcal/mol, respectively. MD simulation results were compared using binding free-energy estimates to validate the findings (**Fig. 9 and Table S7**).

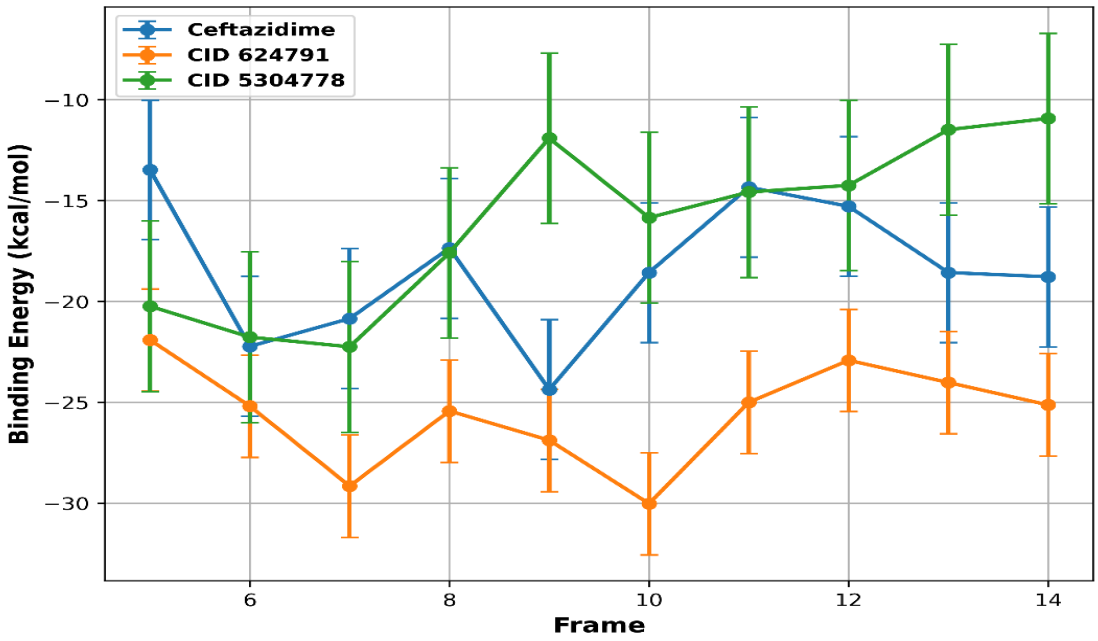


Fig. 9. MM-PBSA binding free energy (ΔG_bind) of protein–ligand complexes calculated from the final 20 ns of MD simulations. Ceftazidime, CID 624791, and CID 5304778 are compared, where a lower ΔG_bind indicates stronger binding affinity.

The free energy landscape (FEL) plots illustrate the systems of Apo (**Fig. 10A**), Ceftazidime (**Fig. 10B**), CID 624791 (**Fig. 10C**), and CID 5304778 (**Fig. 10D**), using RMSD and Rg as reaction coordinates. The Gibbs free energy values range from 0 to 5.88 kcal/mol for the Apo and ceftazidime, 0 to 5.95 kcal/mol for CID 624791, and 0 to 6.21 kcal/mol for CID 5304778. The Apo's main free energy basin appears at RMSD values between 0.09 and 0.18 nm and Rg values between 1.75 and 1.81 nm. In the ceftazidime complex, the free-energy basin was observed at RMSD values of 0.07-0.28 nm and Rg values of 1.77-1.87 nm. For the CID 624791complex, multiple favorable free energy basins were observed, with RMSD values ranging from 0.078 to 0.19 nm and Rg values between 1.77 and 1.83 nm. Similarly, the complex containing CID 5304778 showed free-energy basins with Rg values between 1.78 and 1.87 nm and RMSD values of approximately 0.07-0.25 nm, highlighting the stable conformational states of the protein–ligand complexes.

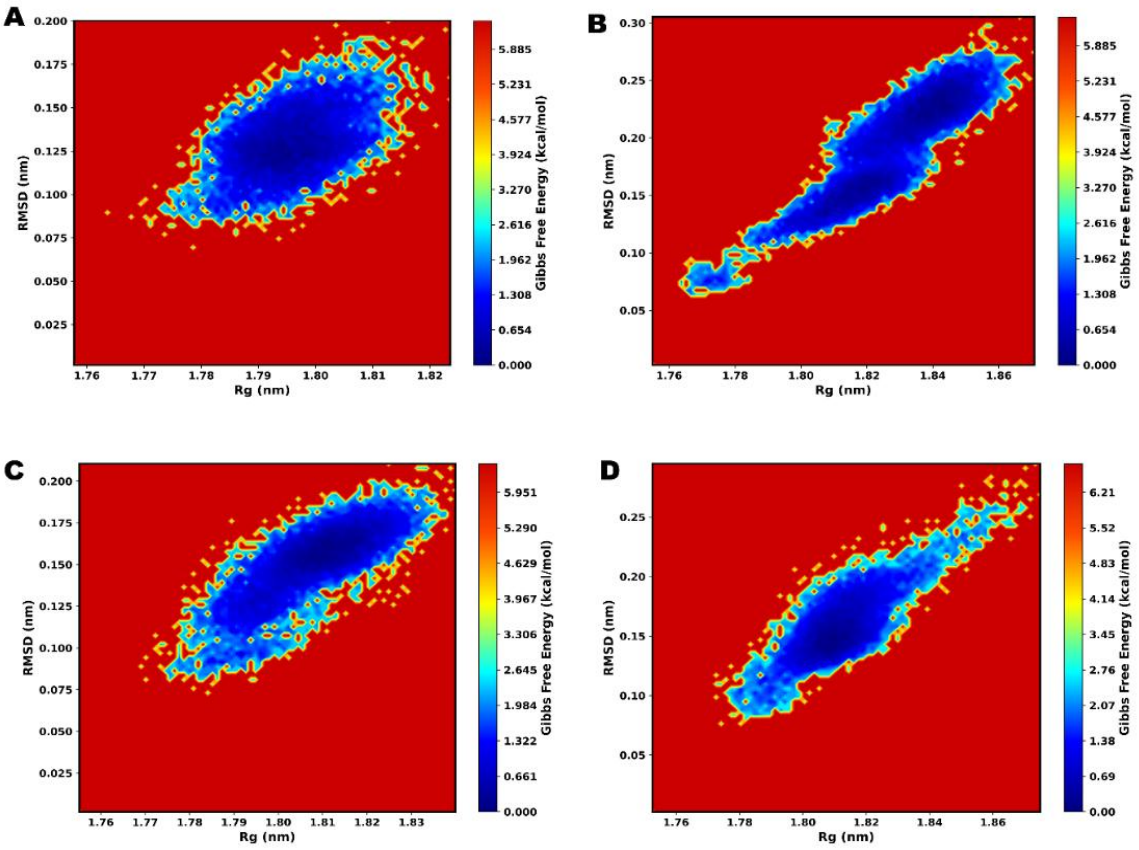


Fig. 10. FEL profiles of the Apo and ligand-bound systems. (A) Apo, (B) Ceftazidime-bound complex, (C) CID 624791-bound complex, and (D) CID 5304778-bound complex.

Principal component analysis

In Principal component analysis (PCA), the first two principal components, PC1 and PC2, capture the most significant structural variations induced by ligand binding and account for most of the motion variance. For the Apo system (**Fig. 11A**), the PC1 vs. PC2 plot shows the distribution of conformational states, with PC1 accounting for 22.89% of the total variance and PC2 for 11.12%, indicating distinct conformational states. The PC2 vs. PC3 plot provides a three-dimensional representation of the conformational distribution, with PC3 contributing 5.31% of the variance. The eigenvalue rank plot further indicates that PC1, PC2, and PC3 contribute 22.89%, 11.12%, and 5.31% of the total variance, respectively. In addition, the PC1 vs. PC3 plot illustrates the distribution of conformations along PC1 and PC3. For the complex containing Ceftazidime with the 1YLY PDB structure (**Fig. 11B**), the PC1 vs. PC2 plot indicates that PC1 accounts for 37.86% of the variance, while PC2 accounts for 11.12%, reflecting distinct conformational states. The PC2 vs. PC3 plot illustrates the distribution of PC2 and PC3, with PC3 contributing approximately 6.55% of the variance. According to the eigenvalue rank plot, PC1, PC2, and PC3 account for 37.86%, 11.12%, and 6.55% of the total variance, respectively, while the PC1 vs. PC3 plot shows the conformational distribution along these two components. The complex containing CID 624791 (**Fig. 11C**) shows that PC1 explains 17.82% of the variance and PC2 explains 14.53%, indicating the presence of different conformational clusters. The PC2 vs. PC3 plot shows the relationship

between PC2 and PC3, with PC3 accounting for 5.87% of the variance. The eigenvalue rank plot shows that PC1, PC2, and PC3 contribute 17.82%, 14.53%, and 5.87% of the total variance, respectively, while the PC1 vs. PC3 plot illustrates the distribution of conformations along PC1 and PC3. Similarly, in the PCA results for CID 5304778 with the 1YLY PDB structure (**Fig. 11D**), the PC1 vs. PC2 plot reveals distinct conformational states, with PC1 accounting for 25.67% of the variance and PC2 for 13.50%. The PC2 vs. PC3 plot shows the distribution between PC2 and PC3, with PC3 contributing approximately 6.33% of the variance. The eigenvalue rank plot indicates that PC1, PC2, and PC3 account for 25.67%, 13.50%, and 6.33% of the total variance, respectively, and the PC1 vs. PC3 plot further illustrates the conformational distribution along these two principal components.

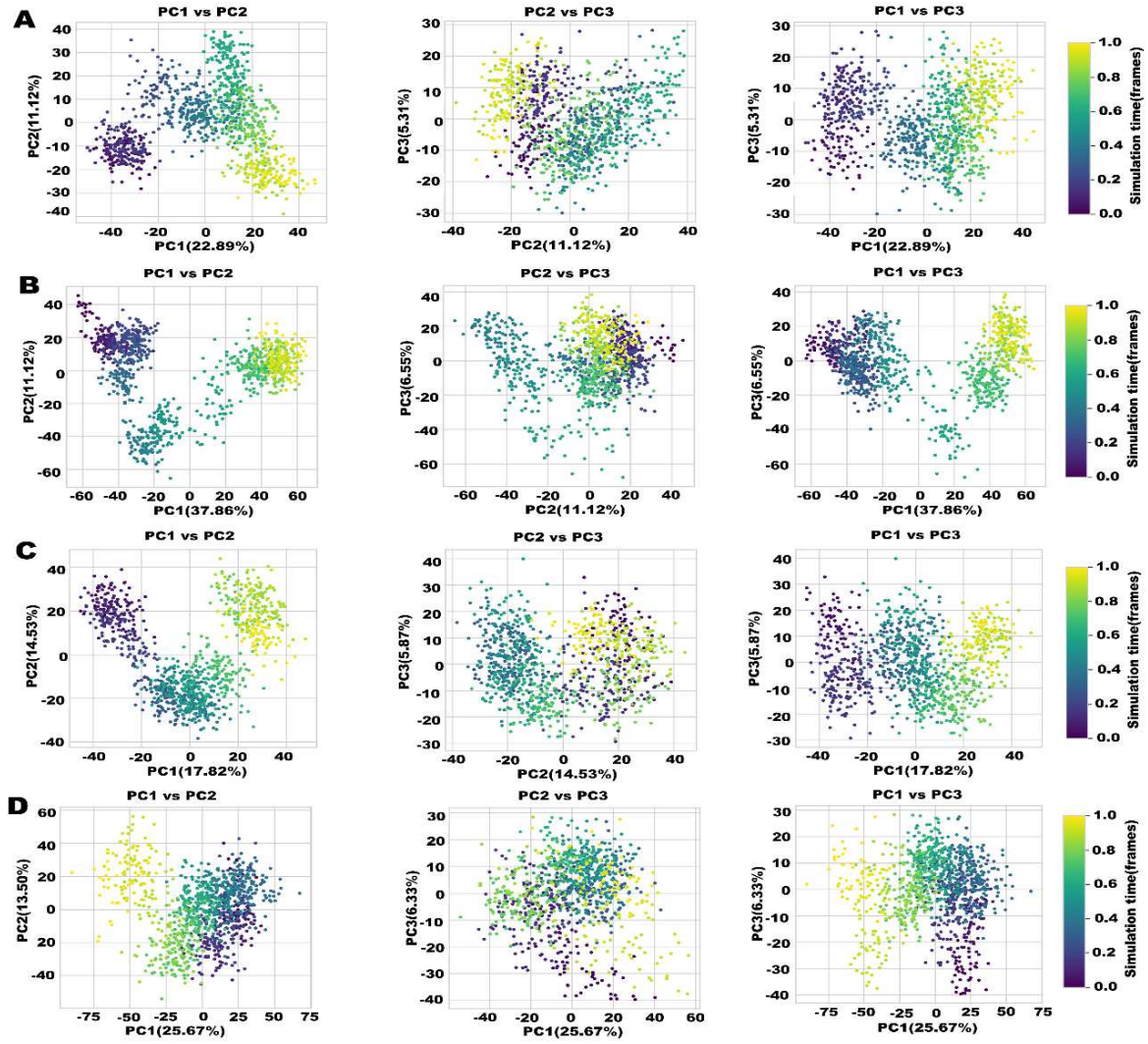


Fig. 11. PCA of the protein (PDB ID: 1YLY) in Apo and ligand-bound states, illustrating the global conformational dynamics and structural flexibility. (A) Apo system, (B) Ceftazidime-bound complex, (C) CID 624791-bound complex, and (D) CID 5304778-bound complex. For each system, the PC1 vs. PC2, PC2 vs. PC3, and PC1 vs. PC3 plots depict the distribution of conformational states, while the eigenvalue rank plots represent the percentage contribution of the principal components to the total motion variance.

Dynamic cross-correlation matrix (DCCM) analysis

The dynamic relationships among residues throughout the entire simulation were visualized using two-dimensional DCCM plots (**Fig. 12**). DCCM values ranged from −1.0 to 1.0 and were represented by a color gradient from blue to red. Different color intensities were used to represent the degree of correlation between residues, with darker colors indicating stronger correlations. Positive correlations (0 to 1) represent residues moving in the same direction, whereas negative correlations (−1 to 0) indicate motions in opposite directions. A comparison of the DCCM maps shows that the correlation patterns of the systems Apo (**Fig. 12A**), CID 624791 (**Fig. 12C**), and CID 5304778 (**Fig. 12D**) differ noticeably from the ceftazidime system (**Fig. 12B**). As highlighted by the black dashed boxes, these systems exhibit a considerable increase in positively correlated motions compared with the standard. The structures associated with CID 624791 and CID 5304778 demonstrate a more pronounced expansion of correlated regions. Moreover, DCCM plots indicate clear differences in correlation patterns between the CID 62479 and CID 5304778 systems. Although the overall positively correlated motions in the CID 62479 system remain relatively similar to the standard, the negatively correlated motions are markedly reduced in the CID 5304778 system.

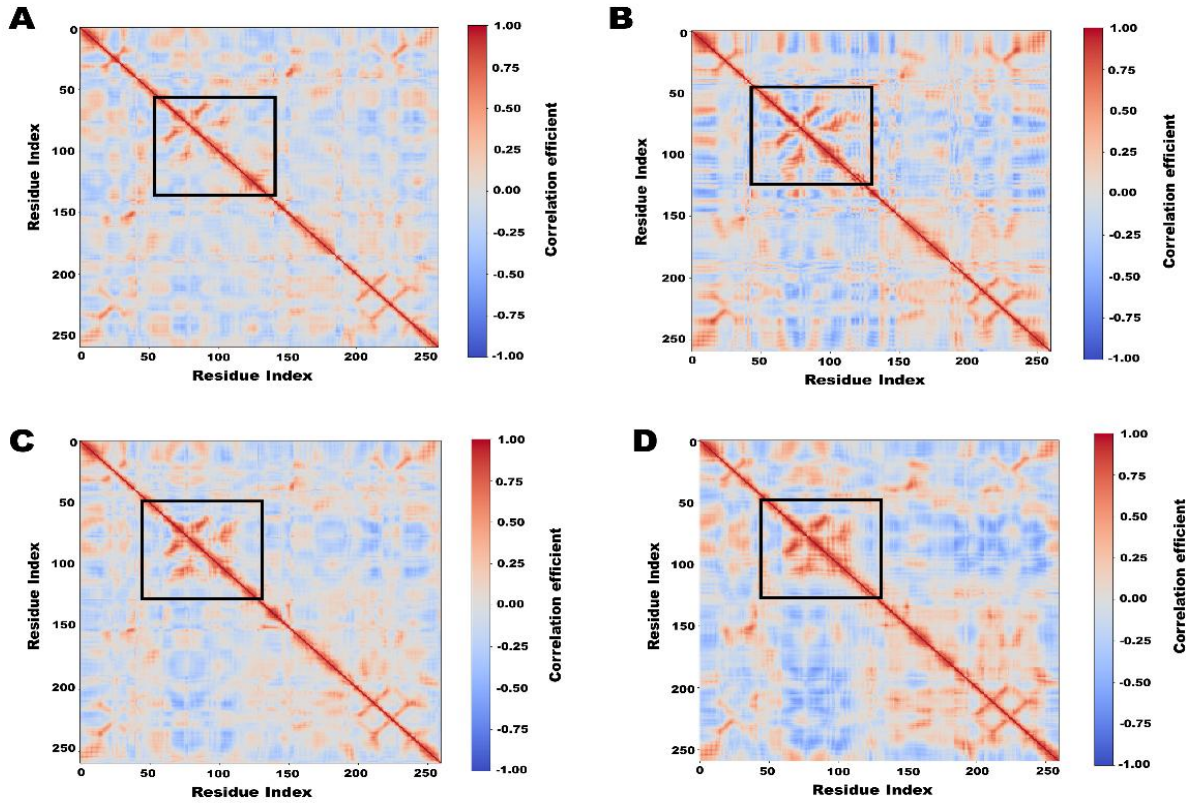


Fig. 12. DCCM analysis from the molecular dynamics simulations. (A) Apo, (B) Ceftazidime-bound (standard), (C) CID 624791-bound, and (D) CID 5304778-bound systems. The color scale ranges from −1.0 (blue, anti-correlated motions) to 1.0 (red, positively correlated motions), with intensity reflecting the strength of residue–residue correlations.

Discussion

The rapid rise of MDR pathogens poses a significant global health concern, lowering the effectiveness of conventional antibiotics and underscoring the urgent need for new therapeutic approaches. In this regard, bioactive compounds from plants have gained increasing attention due to their structural diversity, low toxicity, and potential to act synergistically with known antibacterial drugs [6, 15]. The biological activities of plant materials are due to the secondary metabolites synthesized in plant cells. Among these compounds, plant-derived antioxidants, especially polyphenols, have been widely reported to have a diverse range of pharmacological properties, including antimicrobial, anti-inflammatory, and cardioprotective effects through mechanisms such as lowering blood pressure, improving cholesterol profiles, and mitigating oxidative stress [52, 53]. The present investigation revealed significant antibacterial, antifungal, and allelopathic properties in *Cassia sophera* extracts, which support their traditional medical use and suggest they could be a potential source of new antimicrobial agents.

The antibacterial assessment of *C. sophera* extracts exhibited significant solvent- and concentration-dependent inhibitory effects against both Gram-positive and Gram-negative bacteria. The highest antibacterial activity was observed in the methanolic fraction, with a larger zone of inhibition, particularly against *Escherichia coli* and *Staphylococcus gallinarum*. Chloroform extract exhibited modest antibacterial activity, whereas the petroleum benzene extract showed no detectable inhibitory effect against the tested microorganisms. The higher effectiveness of the methanolic extract may be due to the effective extraction of polar bioactive phytochemicals such as phenolics, flavonoids, and alkaloids, which are well known for their antibacterial activities. These chemicals restrict bacterial growth by disrupting cell membrane integrity, inhibiting enzyme function, and interfering with nucleic acid production. Similar results were reported in previous research, in which methanol was an effective solvent for extracting antibacterial secondary metabolites from medicinal plants [54,55.] The dose-dependent increase in zone of inhibition considerably strengthens the antibacterial activity of *C. sophera*. The general trend in antibacterial activity indicated the importance of solvent polarity in extracting the active antimicrobial compounds, consistent with previous phytochemical and antimicrobial investigations [56].

The extracts of *C. sophera* inhibited the development of *Fusarium concentricum* and *Fusarium fujikuroi*. The methanolic extracts demonstrated the most effectiveness against *F. concentricum*, while *F. fujikuroi* was more susceptible to petroleum benzene fractions. Microscopic investigation revealed structural damage in fungal hyphae, such as vacuolation and fragmentation, reflecting loss of cell wall integrity. These results are consistent with the potential of plant phenolics and terpenoids to influence fungal membrane structures and block enzymatic pathways necessary for fungal growth [57,58.] The variation in sensitivity between the two Fusarium species underscores the need for species-specific experiments to evaluate antifungal activity.

In the present study, we investigated the phytotoxic effects of *C. sophera* extracts on 30 BRRI Dhan-28. The germination percentages were similar to or slightly higher in the methanolic extracts than in the control, suggesting that the extracts had a minor effect on the seeds' early metabolic processes. Previous research exhibits dose-dependent biological activity with little phytotoxicity at moderate concentrations [59]. Conversely, chloroform and petroleum benzene extracts induced a marginal reduction in germination, consistent with findings on the inhibitory effects of non-polar allelochemicals on seed physiology. Furthermore, seedling growth was not significantly affected by the methanolic and chloroform treatments, whereas the petroleum benzene extract reduced root elongation at higher concentrations, possibly due to impairment of mitotic activity in root

meristematic tissues, as reported in allelopathic studies with *C. sophera* [60]. Furthermore, the genus *Caesalpinia* contains copious amounts of phenolics and flavonoids with significant antibacterial and other bioactive activities, supporting these findings. The low phytotoxicity, especially of the methanolic fraction, makes it a potential eco-friendly antibacterial agent with minimal impact on crop growth.

Using literature-reported phytocompounds of *C. sophera*, an *in silico* virtual screening against CTX-M-9 β-lactamase (PDB ID: 1YLY) identified CID 624791 and CID 5304778 as exhibiting better binding affinities than the control drug ceftazidime compared. The CTX-M-9 β-lactamase protein remains relatively underexplored as a target for inhibition by phytocompounds through molecular docking approaches. However, a previous molecular modelling study identified two synthetic compounds from DrugBank, DB01753 and ZINC33264777, as potential inhibitors of CTX-M-9 [22]. Both compounds interacted with the 1YLY protein through hydrogen bonding with residues SER237, ASN104, GLU166, SER274, and TYR105 [61]. The lower binding energies and stable interaction patterns observed in this study indicate that CID 624791 and CID 5304778 bind more effectively to the active site of the CTX-M-9 β-lactamase protein than the control compound, ceftazidime, suggesting their potential inhibitory activity.

The ADME analysis was possible to indicate that CID 624791 and CID 5304778 have favorable pharmacokinetic properties, with ideal molecular weight, LogP values, and TPSA, suggesting good membrane permeability and potential oral bioavailability. Both compounds exhibited high projected gastrointestinal (GI) absorption, adequate water solubility, and limited potential for blood-brain barrier (BBB) penetration, reducing the risk of central nervous system-related side effects. The features are in favour of the compounds' drug-likeness and possibility for systemic applications because the compounds showed no predicted hepatotoxicity, carcinogenicity, or mutagenicity. Further, their calculated LD_{50} values are below the permissible safety limits and thus fall under the lower toxicity classifications. The absence of evidence for severe immunotoxicity or cytotoxicity indicates a low risk of harmful effects. Overall, the combined ADME and toxicity analyses indicated that these phytochemicals are bioactive and exhibit drug-like properties, with favorable safety and absorption profiles, supporting their future potential as CTX-M-9 β-lactamase (1YLY) inhibitors in preclinical development.

Frontier molecular orbitals (FMOs) were utilized to evaluate the electronic properties, reactivity, and potential interaction sites of the studied compounds using DFT. The HOMO corresponds to regions of high electron density and electron-donating capability, while the LUMO represents electron-deficient regions favorable for electron acceptance. The HOMO–LUMO energy gap serves as an important descriptor of chemical reactivity and kinetic stability. The global reactivity descriptors indicate that CID 624791 is a promising candidate, comparable to Ceftazidime, and exhibits an optimal balance between sufficient reactivity and desirable stability.

MD simulations provide insight into the conformational stability and flexibility of protein-ligand complexes over time and mimic settings that closely resemble the physiological milieu of the human body [62]. Detailed knowledge of conformational stability and dynamic behaviour of 1YLY protein-ligand complexes was obtained by MD simulations on a time scale of 100 ns. The analysis of key parameters such as RMSD, RMSF, Rg, SASA, DCCM, FEL, and PCA helped to comprehend the structural aspects and dynamic behaviors of these complexes. RMSD analysis provides insight into the overall stability of the protein-ligand complexes, whereas RMSF is used to assess the dynamic flexibility of individual amino acid residues throughout the ligand-binding process [63]. The RMSD and RMSF values of the selected compounds, CID 624791 and CID

5304778, were lower than those of the control compound, ceftazidime, over the 100 ns simulation, indicating enhanced structural stability and reduced residue fluctuations in the CTX-M-9 β-lactamase protein–ligand complexes. The lower Rg is a sign of a more compact structure of the protein–ligand complex, while higher Rg values imply a higher probability of ligand dissociation from the protein [60]. The Rg values of CID 624791 and CID 5304778 were lower than those of the control ceftazidime. A lower SASA value is indicative of a more compact protein-ligand complex with stronger connections between the amino acid residues and the surrounding water molecules, whereas a larger value is indicative of a diminished structural integrity. In this study, the complexes of CID 624791 and CID 5304778 with CTX-M-9 β-lactamase showed lower SASA values than the protein–ceftazidime complex, indicating increased structural stability and tighter binding contacts.

The MM-PBSA analysis demonstrated that CID 624791 exhibited the most negative ΔG value, indicating the strongest binding affinity compared to the control and CID 5304778. However, CID 5304778 demonstrated a comparatively weaker binding energy, suggesting reduced thermodynamic favorability despite maintaining structural stability during simulation. Favorable and stable binding contacts were indicated by a greater negative ΔG value [64.]

Furthermore, FEL analysis of CID 62479 and CID 5304778 revealed the most stable binding conformation, whereas the reference and Apo molecule displayed significant instability. The most stable conformational states of the complexes were identified by extracting the lowest-energy snapshots from the free energy basins [65].

The PCA explaining the largest proportion of variance reflects the dominant motion within the system. PCA analysis revealed that CID 624791 induced the most stable conformational dynamics in the protein–ligand system, characterized by reduced dominance of a single principal motion and a more uniform distribution across multiple eigenvectors. In comparison, Ceftazidime showed a highly PC1-dominant motion profile, indicating stronger directional restriction, while CID 5304778 showed intermediate behavior. Overall, CID 624791 demonstrated the most favorable dynamic adaptation within the binding pocket. Furthermore, the observed decrease in negative correlations may contribute to increased structural stability of the protein [66].

In recent studies, the synthetic compounds DB01753 and ZINC33264777 (DrugBank) inhibit the β-lactamase CTX-M-9, but these inhibitors are generally limited by selectivity, resistance, and safety concerns [67]. In contrast, our computational study identified the plant-derived compound CID 624791 as a potential inhibitor of CTX-M-9 β-lactamase, with stable interactions and pharmacokinetic properties. These findings suggest that CID 624791 may be a candidate for further investigation against the CTX-M-9 β-lactamase. Future studies should experimentally validate its inhibitory activity, elucidate its mechanism of action, and evaluate its pharmacokinetic and pharmacodynamic properties *in vivo*. Moreover, investigating its potential alongside conventional antibiotics may provide a feasible approach to combat antibiotic resistance and reduce required drug doses.

Conclusion

Sequential extracts of *Cassia sophera* showed significant antibacterial activity against multidrug-resistant *E. coli* and *S. aureus* and remarkable antifungal activity against *Fusarium concentricum* and *F. fujikuroi*, varying with the polarity of the solvents and the type of fungi. The methanolic extract also had a favorable seed germination rate in BRRI Dhan-28, which showed low phytotoxicity. The in silico analysis predicted high binding affinity and favorable interactions

between the selected phytocompounds from *C. sophera* and the target CTX-M-9 β-lactamase (PDB ID: 1YLY), which hydrolyzes penicillins and cephalosporins. ADMET profiling revealed that the two compounds, CID 624791 and CID 5304778, exhibited favorable pharmacokinetics and low toxicity, and molecular dynamics simulations further validated their stability. This stability was confirmed by MM-PBSA analysis, indicating that the compound exhibits a strong, stable interaction with the target enzyme. Furthermore, DFT analysis identified CID 624791 as a potential lead candidate for further investigation and optimization. Nevertheless, these computational findings require experimental validation, including *in vitro* enzymatic inhibition assays and subsequent *in vivo* studies, to determine whether these compounds can effectively inhibit CTX-M-9.

Acknowledgments

The authors acknowledge the use of artificial intelligence tools to improve the grammar, language, and clarity of this manuscript. The AI tool was used solely for language editing.

Author contributions

MSH, KAE, MAM and MNHJ conducted experimental work, performed data analysis and prepared the initial draft of the manuscript. MMHS, MNR, CB, MSA and AS were involved in formal analysis, data curation, and manuscript reviewing. NI validated data, reviewed and edited the manuscript. MN and MFH were involved in the project's conceptual framework and overall study design, supervision, reviewing and editing the manuscript. All authors read and approved the final version of the manuscript.

Funding

No funding was received for conducting this study.

Declarations

Competing interests

The authors declare no competing interests.

Ethical approval and consent to participate

Not applicable.

Consent for publication

Not applicable.

Data availability

All datasets on which the conclusions of the manuscript rely are presented in the main paper and additional supplementary files.

Plant collection approval

No approval is needed from the authority in Bangladesh to collect *Cassia sophera* for research purposes.

IUCN Policy statement

The collection of plant material complied with relevant institutional, national, and international guidelines and legislation.

References

1. Walsh TR, Gales AC, Laxminarayan R, Dodd PC. Antimicrobial resistance: addressing a global threat to humanity. PLoS Med 2023;20:e1004264.
2. Naghavi M, Vollset SE, Ikuta KS, Swetschinski LR, Gray AP, Wool EE, et al. Global burden of bacterial antimicrobial resistance 1990–2021: a systematic analysis with forecasts to 2050. The Lancet 2024;404:1199–226.
3. Tang KWK, Millar BC, Moore JE. Antimicrobial Resistance (AMR). Br J Biomed Sci. 2023;80:11387. doi: 10.3389/bjbs.2023.11387.
4. Agriopoulou S, Stamatelopoulou E, Varzakas T. Advances in occurrence, importance, and mycotoxin control strategies: Prevention and detoxification in foods. Foods 2020;9:137.
5. D. Steve, E. M. Kiarii, M. W. Kiarie, J. N. Nyariki, Emergence and spread of multidrug-resistant pathogens: A global health challenge. Mass Gathering Medicine 2026;5:100050. DOI. 10.1016/j.mgmed.2026.100050
6. Zothantluanga JH, Abdalla M, Rudrapal M, Tian Q, Chetia D, Li J. Computational investigations for identification of bioactive molecules from *Baccaurea ramiflora* and *Bergenia ciliata* as inhibitors of SARS-CoV-2 Mpro. Polycycl Aromat Compd 2023;43:2459–87.
7. Wagner H. Synergy research: approaching a new generation of phytopharmaceuticals. Fitoterapia 2011;82:34–7.
8. Gupta RK. Medicinal and Aromatic Plants with Colour Plates: Traditional and Commercial Uses Agrotechniques Biodiversity Conservation. CBS; 2010.
9. Rahman MM, Rahman MM, Islam MR, Rahman A, Rahman MS. Characterization of clinical bacteria and their control by a medicinal plant (Cassia Sophera L.) extracts. J Char Dev Nov Mater 2009;1:159–68.
10. Rahman A, Rahman MM, Sheik MMI, Rahman MM, Shadli SM, Alam MF. Free radical scavenging activity and phenolic content of Cassia sophera L. Afr J Biotechnol 2008;7:1591.
11. Tripathi AK, Kohli S. Pharmacognostic and phytochemical studies on the flowers of Punica granatum. Int J Pharm Res Dev 2012;3:1–7.
12. Deshpande S. Evaluation of in vitro antimicrobial activity of extracts from Cassia obtusifolia L. and Senna sophera (L.) Roxb against pathogenic organisms. J Appl Pharm Sci 2016.
13. Asimi OA, Sahu NP, Pal AK. Antioxidant activity and antimicrobial property of some Indian spices. International Journal of Scientific and Research Publications 2013;3:1–8.
14. Rahman A, Rahman MM, Sheik MMI, Rahman MM, Shadli SM, Alam MF. Free radical scavenging activity and phenolic content of Cassia sophera L. Afr J Biotechnol 2008;7:1591.
15. Ayaz M, Ullah F, Sadiq A, Ullah F, Ovais M, Ahmed J, et al. Synergistic interactions of phytochemicals with antimicrobial agents: Potential strategy to counteract drug resistance. Chem Biol Interact 2019;308:294–303.

16. Devasia J, Chinnam S, Khatana K, Shakya S, Joy F, Rudrapal M, et al. Synthesis, DFT and in silico anti-COVID evaluation of novel tetrazole analogues. Polycycl Aromat Compd 2023;43:1941–56.

17. Salo-Ahen OMH, Alanko I, Bhadane R, Bonvin AMJJ, Honorato RV, Hossain S, et al. Molecular dynamics simulations in drug discovery and pharmaceutical development. Processes 2020;9:71.

18. Abdullahi M, Shallangwa GA, Uzairu A. In silico QSAR and molecular docking simulation of some novel aryl sulfonamide derivatives as inhibitors of H5N1 influenza A virus subtype. Beni Suef Univ J Basic Appl Sci 2020;9:2.

19. Sidjabat HE, Paterson DL. Multidrug-resistant Escherichia coli in Asia: epidemiology and management. Expert Rev Anti Infect Ther 2015;13:575–91.

20. Szmolka A, Nagy B. Multidrug resistant commensal Escherichia coli in animals and its impact for public health. Front Microbiol 2013;4:258.

21. Judge A, Hu L, Sankaran B, Van Riper J, Venkataram Prasad B V, Palzkill T. Mapping the determinants of catalysis and substrate specificity of the antibiotic resistance enzyme CTX-M β-lactamase. Commun Biol 2023;6:35.

22. Chen Y, Shoichet B, Bonnet R. Structure, function, and inhibition along the reaction coordinate of CTX-M β-lactamases. J Am Chem Soc 2005;127:5423–34.

23. Hosen E, Tasnim F, Nesa M, Rahman S, Hasan F, Zaman R. Antibacterial activity of black and green tea extracts against multridrug resistance Shigella sonnei and Shigella flexneri: an integrated experimental study and computational approach. World Joural Pharm Pharm Sci 2021;10:1663–86.

24. Basra SMA, Farooq M, Tabassam R, Ahmad N. Physiological and biochemical aspects of pre-sowing seed treatments in fine rice (Oryza sativa L.). Seed Science and Technology 2005;33:623–8.

25. Tian W, Chen C, Lei X, Zhao J, Liang J. CASTp 3.0: computed atlas of surface topography of proteins. Nucleic Acids Res 2018;46:W363–7.

26. Sarkar KK, Mitra T, Rahman MA, Raja IM, Aktaruzzaman M, Abid MA, et al. In vivo bioactivities of Hoya parasitica (Wall.) and in silico study against cyclooxygenase enzymes. Biomed Res Int 2022;2022:1331758.

27. Lyne PD, Lamb ML, Saeh JC. Accurate prediction of the relative potencies of members of a series of kinase inhibitors using molecular docking and MM-GBSA scoring. J Med Chem 2006;49:4805–8.

28. Daina A, Michielin O, Zoete V. Sci Rep. 2017, 7, 42717. DOI: Https://Doi Org/101038/Srep42717 2024.

29. Pires DE V, Kaminskas LM, Ascher DB. Prediction and optimization of pharmacokinetic and toxicity properties of the ligand. Computational drug discovery and design, Springer; 2018, p. 271–84.

30. Wang E, Sun H, Wang J, Wang Z, Liu H, Zhang JZH, et al. End-Point Binding Free Energy Calculation with MM/PBSA and MM/GBSA: Strategies and Applications in Drug Design. Chem Rev 2019;119:9478–508. https://doi.org/10.1021/acs.chemrev.9b00055.

31. Terefe EM, Ghosh A. Molecular Docking, Validation, Dynamics Simulations, and Pharmacokinetic Prediction of Phytochemicals Isolated From Croton dichogamus Against the HIV-1 Reverse Transcriptase. Bioinform Biol Insights 2022;16. https://doi.org/10.1177/11779322221125605.

32. Benarous N, Cherouana A, Aubert E, Durand P, Dahaoui S. Synthesis, characterization, crystal structure and DFT study of two new polymorphs of a Schiff base (E)-2-((2, 6-dichlorobenzylidene) amino) benzonitrile. J Mol Struct 2016;1105:186–93.

33. Meenakshi R. Spectral investigations, DFT based global reactivity descriptors, Inhibition efficiency and analysis of 5-chloro-2-nitroanisole as π-spacer with donor-acceptor variations effect for DSSCs performance. J Mol Struct 2017;1127:694–707.

34. Frisch M, Trucks G, Schlegel HB, Scuseria G, Robb M, Cheeseman J, et al. Gaussian 09, Revision a. 02, 200, gaussian. Inc, Wallingford, CT 2009;271.

35. Tirado-Rives J, Jorgensen WL. Performance of B3LYP density functional methods for a large set of organic molecules. J Chem Theory Comput 2008;4:297–306.

36. Rahman MS, Rana MS, Azbar Rayhan NM, Emad AH, Matin SB, Kudrat-E-Zahan M, et al. Synthesis, characterization, DFT studies, target prediction, molecular docking, and ADMET properties of the Schiff base 2-[2-[(2-Hydroxyphenyl) methylideneamino] ethyliminomethyl] phenol and its Ni (II) and Co (II) complexes. Spectroscopy Letters 2025:1–27.

37. Karplus M, Petsko GA. Molecular dynamics simulations in biology. Nature 1990;347:631–9.

38. Hess B, Bekker H, Berendsen HJC, Fraaije JGEM. LINCS: A linear constraint solver for molecular simulations. J Comput Chem 1997;18:1463–72.

39. Darden T, York D, Pedersen L. Particle mesh Ewald: An N log (N) method for Ewald sums in large systems. Journal of Chemical Physics 1993;98:10089–92.

40. Hassan NM, Alhossary AA, Mu Y, Kwoh C-K. Protein-ligand blind docking using QuickVina-W with inter-process spatio-temporal integration. Sci Rep 2017;7:15451.

41. Moman RN, Gupta N, Varacallo M. Physiology, Albumin. StatPearls 2021.

42. Bussi G, Donadio D, Parrinello M. Canonical sampling through velocity rescaling. J Chem Phys 2007;126.

43. Berendsen HJC, Postma JPM van, Van Gunsteren WF, DiNola A, Haak JR. Molecular dynamics with coupling to an external bath. J Chem Phys 1984;81:3684–90.

44. Hess B, Bekker H, Berendsen HJC, Fraaije JGEM. LINCS: A linear constraint solver for molecular simulations. J Comput Chem 1997;18:1463–72.

45. Kim GB, Seo JI, Gye MC, Yoo HH. Isosorbide, a versatile green chemical: Elucidating its ADME properties for safe use. Ecotoxicol Environ Saf 2024;272:116051.

46. Haloui A, Arfaoui Y. A DFT study of the conformational behavior of para-substituted acetophenones in vacuum and in various solvents. Journal of Molecular Structure: THEOCHEM 2010;950:13–9.

47. Ali MA, Sheikh H, Yaseen M, Faruqe MO, Ullah I, Kumar N, et al. Exploring the therapeutic potential of Petiveria alliacea L. phytochemicals: A computational study on inhibiting SARS-CoV-2's main protease (Mpro). Molecules 2024;29:2524.

.48 Katiyar RS, Jha PK. Molecular simulations in drug delivery: Opportunities and challenges. Wiley Interdiscip Rev Comput Mol Sci 2018;8:e1358.

49. Hossain A, Hossan MS, Prodhan MS, Joy MNH, Siam MR, Rahman ME, et al. Uralenol, Glycyrol, and Abyssinone II as potent inhibitors of fibroblast growth factor receptor 2 from anti-cancer plants: A deep learning and molecular dynamics approach. PLoS One 2026;21:e0341498.

50. Maria-Solano MA, Serrano-Hervás E, Romero-Rivera A, Iglesias-Fernández J, Osuna S. Role of conformational dynamics in the evolution of novel enzyme function. Chemical Communications 2018;54:6622–34.

51. Akash S, Bayıl I, Mahmood S, Mukerjee N, Mili TA, Dhama K, et al. Mechanistic inhibition of gastric cancer-associated bacteria Helicobacter pylori by selected phytocompounds: A new cutting-edge computational approach. Heliyon 2023;9.

52. Manach C, Scalbert A, Morand C, Rémésy C, Jiménez L. Polyphenols: food sources and bioavailability. Am J Clin Nutr 2004;79:727–47.

53. Giglio R V, Patti AM, Cicero AFG, Lippi G, Rizzo M, Toth PP, et al. Polyphenols: potential use in the prevention and treatment of cardiovascular diseases. Curr Pharm Des 2018;24:239–58.

54. Mehmood A, Javid S, Khan MF, Ahmad KS, Mustafa A. In vitro total phenolics, total flavonoids, antioxidant and antibacterial activities of selected medicinal plants using different solvent systems. BMC Chem 2022;16:64.

55. Cowan MM. Plant products as antimicrobial agents. Clin Microbiol Rev 1999;12:564–82.

56. Kumari K, Adhikari P, Pandey A, Samant SS, Lal M, Pande V. Influence of solvent polarity on phytochemicals, antioxidants, and antimicrobial properties of Delphinium denudatum: A medicinal herb from sainj valley, himachal pradesh, India. Bioactivities 2024;2:30–40.

57. Kursa W, Jamiołkowska A, Wyrostek J, Kowalski R. Antifungal effect of plant extracts on the growth of the cereal pathogen Fusarium spp.—an in vitro study. Agronomy 2022;12:3204.

58. Lagrouh F, Dakka N, Bakri Y. The antifungal activity of Moroccan plants and the mechanism of action of secondary metabolites from plants. J Mycol Med 2017;27:303–11.

59. Omer HAA, Caprioli G, Abouelenein D, Mustafa AM, Uba AI, Ak G, et al. Phenolic profile, antioxidant and enzyme inhibitory activities of leaves from two Cassia and two Senna species. Molecules 2022;27:5590.

60. Gulzar A, Siddiqui MB, Bi S. Phenolic acid allelochemicals induced morphological, ultrastructural, and cytological modification on Cassia sophera L. and Allium cepa L. Protoplasma 2016;253:1211–21.

61. Davari K, Nowroozi J, Hosseini F, Akhavan Sepahy A, Mirzaie S. Inhibitor discovery against beta lactamase CTX-M-9 from E. coli by molecular docking, MM/PBSA and molecular dynamics studies. Cellular and Molecular Research 2019;32:19–31.

62. Pavan M, Menin S, Bassani D, Sturlese M, Moro S. Qualitative estimation of protein–ligand complex stability through thermal titration molecular dynamics simulations. J Chem Inf Model 2022;62:5715–28.

63. Pavan M, Menin S, Bassani D, Sturlese M, Moro S. Qualitative estimation of protein–ligand complex stability through thermal titration molecular dynamics simulations. J Chem Inf Model 2022;62:5715–28.

64. Du X, Li Y, Xia YL, Ai SM, Liang J, Sang P, et al. Insights into Protein–Ligand Interactions: Mechanisms, Models, and Methods. International Journal of Molecular Sciences 2016, Vol 17, 2016;17. https://doi.org/10.3390/ijms17020144.

65. Alawi MM, Alyazidi RM, Bajrai LH, Gattan HS, Alandijany TA, Al-Zahrani IA, et al. Structural insights into natural compound inhibitors of the human metapneumovirus nucleocapsid protein via molecular dynamics and free energy landscape analyses. Sci Rep 2025;15. https://doi.org/10.1038/s41598-025-22428-x.

66. Rajput H, Choudhary G, Siddiqui H, Ghosh A, Prajapat M, Prakash A, et al. In silico drug repurposing targeting fusion and nucleoprotein of human metapneumovirus: A step toward pandemic preparedness. Indian J Pharmacol 2025;57:308–21. https://doi.org/10.4103/ijp.ijp_559_25.

67. Pavan M, Menin S, Bassani D, Sturlese M, Moro S. Qualitative estimation of protein–ligand complex stability through thermal titration molecular dynamics simulations. J Chem Inf Model 2022;62:5715–28.

Supplementary Files

This is a list of supplementary files associated with this preprint. Click to download.

- Supplementaryfile.docx